Polar stratospheric nitric acid depletion surveyed from a decadal dataset of IASI total columns

Gaetane Ronsmans[1,a], Catherine Wespes[1,a,*], Lieven Clarisse[1], Susan Solomon[2], Daniel Hurtmans[1], Cathy Clerbaux[1,3], and Pierre-François Coheur[1]

[1]Université libre de Bruxelles (ULB), Spectroscopy, Quantum Chemistry and Atmospheric Remote Sensing (SQUARES), Brussels, Belgium
[2]Department of Earth, Atmospheric and Planetary Sciences, Massachusetts Institute of Technology, Cambridge, Massachusetts, USA
[3]LATMOS/IPSL, Sorbonne Université, UVSQ, CNRS, Paris, France

[*] Corresponding author: Catherine Wespes (catherine.wespes@ulb.be)
[a] Co-first authors

Abstract

In this paper, we exploit the first 10-year data-record (2008-2017) of nitric acid (HNO_3) total columns measured by the IASI-A/Metop infrared sounder, characterized by an exceptional daily sampling and a good vertical sensitivity in the lower-to-mid stratosphere (around 50 hPa), to monitor the ~~causal~~ relationship between the temperature decrease and the observed HNO_3 loss that occurs each year in the Antarctic stratosphere during the polar night. Since the HNO_3 depletion results from the formation of polar stratospheric clouds (PSCs) which trigger the development of the ozone (O_3) hole, its continuous monitoring is of high importance. We verify here, from the 10-year time evolution of HNO_3 together with temperature ~~the pair HNO3 temperature~~ (taken from reanalysis at 50 hPa), the recurrence of specific regimes in the annual cycle of IASI HNO_3 and identify, for each year, the day and the 50 hPa temperature ("drop temperature") corresponding to the onset of strong HNO_3 depletion in the Antarctic winter. Although the measured HNO_3 total column does not allow ~~differentiating~~ the uptake of HNO_3 by different types of PSC particles along the vertical profile to be differentiated, an average drop temperature of 194.2 ± 3.8 K, close to the nitric acid trihydrate (NAT) existence threshold (~195 K at 50 hPa), is found in the region of potential vorticity lower than -10×10^{-5} $K.m^2.kg^{-1}.s^{-1}$ (similar to the 70° – 90° S Eqlat region during winter). The spatial distribution and inter-annual variability of the drop temperature are investigated and discussed. This paper highlights the capability of the IASI sounder to monitor the evolution of polar stratospheric HNO_3, a key player in the processes ~~long-term evolution of the polar stratospheric composition and processes~~ involved in the depletion of stratospheric O_3.

1 Introduction

The cold and isolated air masses found within the polar vortex during winter are associated with a strong denitrification of the stratosphere due to the formation of PSCs (composed of HNO_3, sulphuric acid (H_2SO_4) and water ice (H_2O)) (e.g. Peter, 1997; Voigt et al., 2000; von König, 2002; Schreiner et al., 2003; Peter and Grooß, 2012). These clouds strongly affect the polar chemistry by (1) acting as surfaces for the heterogeneous activation of chlorine and bromine compounds, in turn leading to enhanced O3 destruction (e.g. Solomon, 1999; Wang and Michelangeli, 2006; Harris et al., 2010; Wegner et al., 2012) and by (2) removing gas-phase HNO_3 temporarily or permanently through uptake by PSCs and sedimentation of large PSC particles to lower altitudes. The denitrification of the polar stratosphere during winter delays the reformation of $ClONO_2$, a chlorine reservoir~~s~~, and, hence, intensifies the O_3 hole (e.g. Solomon, 1999; Harris et al., 2010; Tritscher et al., 2021). The heterogeneous reaction rates

on PSCs surfaces and the uptake of HNO$_3$ strongly depend on the temperature and on the PSCs particles type. The PSCs are classified into three ~~3~~different types based on their composition and optical properties: type Ia solid nitric acid trihydrate - NAT (HNO$_3$.(H$_2$O)$_3$), type Ib liquid supercooled ternary solution - STS (HNO$_3$/H$_2$SO$_4$/H$_2$O with variable composition) and type II, crystalline water-ice particles (likely composed of a combination of different chemical phases) (e.g. Toon et al., 1986; Koop et al., 2000; Voigt et al., 2000; Lowe and MacKenzie, 2008). In the stratosphere, they mostly consist of mixtures of liquid/solid STS/NAT particles in varying number densities, with HNO$_3$ being the major constituent of these particles. The large-size NAT particles of low number density are the principal cause of sedimentation (Lambert et al., 2012; Pitts et al., 2013; Molleker et al., 2014; Lambert et al., 2016). The formation temperature of STS (T$_{STS}$) and the thermodynamic equilibrium temperatures of NAT (T$_{NAT}$) and ice (T$_{ice}$), have been determined, respectively, as: ~192 K (Carslaw et al., 1995), ~195.7 K (Hanson and Mauersberger, 1988) and ~188 K (Murphy and Koop, 2005) for typical 50 hPa atmospheric conditions (5 ppmv H$_2$O and 10 ppbv HNO$_3$). While the NAT nucleation was thought to require pre-existing ice nuclei, hence, temperatures below T$_{ice}$ ~~and pre-existing ice particles~~ (e.g. Zondlo et al., 2000; Voigt et al., 2003), recent observational and modelling studies have shown that HNO$_3$ starts to condense in early PSC season in liquid NAT mixtures well above T$_{ice}$ (~4 K below T$_{NAT}$, close to T$_{STS}$) even after a very short temperature threshold exposure (TTE) to these temperatures but also slightly below T$_{NAT}$ after a long TTE, whereas the NAT existence persists up to T$_{NAT}$ (Pitts et al., 2013; Hoyle et al., 2013; Lambert et al., 2016; Pitts et al., 2018). It has been recently proposed that the higher temperature condensation results from heterogeneous nucleation of NAT on meteoritic dust in liquid aerosol (Voigt et al., 2005; Hoyle et al., 2013; Grooß et al., 2014; James et al., 2018; Tritscher et al., 2021). Further cooling below T$_{STS}$ and T$_{ice}$ leads to nucleation of liquid STS, of solid NAT onto ice and of ice particles mainly from STS (type II PSCs) (Lowe and MacKenzie, 2008). The formation of NAT and ice has also been shown to be triggered by stratospheric mountain-waves (Carslaw et al., 1998; Hoffmann et al., 2017). Although the formation mechanisms and composition of STS droplets in stratospheric conditions are well described (Toon et al., 1986; Carslaw et al., 1995; Lowe and MacKenzie, 2008), the NAT and ice nucleation processes still require further investigation (Tritscher et al., 2021). This could be important as the chemistry-climate models (CCMs) generally oversimplify the heterogeneous nucleation schemes for ~~the~~ PSCs formation (Zhu et al., 2015; Spang et al., 2018; Snels et al., 2019), preventing an accurate estimation of O$_3$ levels. ~~The influence of HNO$_3$ in modulating O$_3$ abundances in the stratosphere is furthermore underrepresented in CCMs (Kvissel et al., 2012).~~

Several satellite instruments have measured stratospheric HNO$_3$ over decades (e.g. MLS/UARS (Santee et al., 1999), MLS/Aura (Santee et al., 2007), MIPAS/ENVISAT (Piccolo and Dudhia, 2007), ACE-FTS/SCISAT (Sheese et al., 2017) and SMR/Odin (Urban et al., 2009)). ~~The spaceborne lidars CALIOP/CALIPSO and the infrared instrument MIPAS/Envisat) are capable to detect and classify the PSC types, and to follow their formation mechanisms (Lambert et al., 2016; Pitts et al., 2018; Spang et al., 2018) and references therein, which complements in situ measurements (Voigt et al., 2005) and ground-based lidar (Snels et al., 2019).~~ Spaceborne instruments such as the CALIOP/CALIPSO lidar and MIPAS/Envisat measuring in the infrared are capable of detecting and classifying PSC types, allowing their formation mechanisms to be investigated (Lambert et al., 2016; Pitts et al., 2018; Spang et al., 2018, Tritscher et al., 2021 and references therein); these satellite data complement in situ measurements (Voigt et al., 2005) and ground-based lidar (Snels et al., 2019). From these available observational datasets, the HNO$_3$ depletion has been linked to ~~the~~ PSCs formation and detected below the T$_{NAT}$ threshold (Santee et al., 1999; Urban ~~55~~ et al., 2009; Lambert et al., 2016; Ronsmans et al., 2018), but its relationship to PSCs still needs further investigation given the complexity of the nucleation mechanisms that depend~~s~~ on a series of parameters (e.g. atmospheric temperature, water and HNO$_3$ vapour pressure, time exposure to temperatures, temperature history).

In contrast to the limb satellite instruments mentioned above, the infrared nadir sounder IASI offers a dense spatial sampling of the entire globe, twice a day (Section 2). While it cannot provide a vertical profile of HNO_3 similar to that from the limb sounders, IASI provides reliable total column measurements of HNO_3 characterized by a maximum sensitivity in the low-middle stratosphere around 50 hPa (20 km) during the dark Antarctic winter (Ronsmans et al., 2016, 2018) where the PSCs cloud form (Voigt et al., 2005; Lambert et al., 2012; Spang et al., 2016, 2018). This study aims to explore the 10-years continuous HNO_3 measurements from IASI to provide for providing a long-term global picture of depletion and of its dependence to temperatures during polar winter (Section 3). The temperature corresponding to the onset of the strong depletion in HNO_3 records (here referred to as 'drop temperature') is identified in Section 4 for each observed year and discussed in the context of previous studies.

2 Data

The HNO_3 data used in the present study are obtained from measurements of the Infrared Atmospheric Sounding Interferometer (IASI) embarked ononboard the Metop-A satellite. IASI measures the Earth's and atmosphere's radiation in the thermal infrared spectral range (645 - 2760 cm^{-1}), with a 0.5 cm^{-1} apodized resolution and a low radiometric noise (Clerbaux et al., 2009; Hilton et al., 2012). Thanks to its polar sun-synchronous orbit with more than 14 orbits a day and a field of view of four simultaneous footprints of 12 km at nadir, IASI provides global coverage twice a day (9.30 AM and PM mean local solar time). That extensive spatial and temporal sampling in the polar regions is key to this study.

The HNO_3 vertical profiles are retrieved on a uniform vertical 1 km grid of 41 layers (from the surface to 40 km with an extra layer above to 60 km) in near-real-time by the Fast Optimal Retrieval on Layers for IASI (FORLI) software, using the optimal estimation method (Rodgers, 2000). Detailed information on the FORLI algorithm and retrieval parameters specific to HNO_3 can be found in previous papers (Hurtmans et al., 2012; Ronsmans et al., 2016). For this study, only the total columns (v20151001) are used, considering (1) the low vertical resolution of IASI with only one independent piece of information (full width at half maximum - FWHM - of the averaging kernels of ~30 km), (2) the limited sensitivity of IASI to tropospheric HNO_3, (3) the dominant contribution of the stratosphere to the HNO_3 total column and (4) the largest sensitivity of IASI in the region of interest, i.e. in the low and mid-stratosphere (from ~70 to ~30 hPa), where the HNO_3 abundance is the highest (Ronsmans et al., 2016). The IASI measurements capture the expected variations of HNO_3 within the polar night, as illustrated in Fig. 1 that shows examples of vertical HNO_3 profiles retrieved within the dark Antarctic vortex (above Arrival Heights) and outside the vortex (above Lauder). The retrieved profiles are shown along with their associated total retrieval error and averaging kernels (the total column averaging kernels and the so-called "sensitivity profile" are also represented; see Ronsmans et al., 2016 for more details). The total column averaging kernel (in black) indicates the sensitivity of the total column measurement to changes in the vertical distribution of HNO_3, hence, the altitude to which the retrieved total column is mainly sensitive/representative, while the sensitivity profile indicates to which extent the retrieval at one specific altitude comes from the spectral measurement rather than the apriori. Above Arrival Heights during the dark Antarctic winter, we clearly see depleted HNO_3 levels in the low and mid-stratosphere and the altitude of maximum sensitivity (at around 30 hPa for this case (values of ~1 along the total column averaging kernel around that level)). In contrast, Aat Lauder on the contrary, HNO_3 levels larger than the a priori are observed in the stratosphere with a larger range of maximum sensitivity. The total columns are associated with a total retrieval error ranging from around 3% at mid- and polar latitudes (except above Antarctica) to 25% above cold Antarctic surface during winter (due to a weaker sensitivity above very cold surface with a degrees of freedom for signal (DOFS) of 0.95 and to a poor knowledge of the seasonally and wavenumber-dependent emissivity above ice surfaces which induces larger

3

147 forward model errors), and a low absolute bias (smaller~~lower~~ than 12%) in polar regions over the altitude
148 range where the IASI sensitivity is the largest, when compared to ground-based FTIR measurements
149 (see Hurtmans et al., 2012 and Ronsmans et al., 2016 for more details). In order to expand on the
150 comparisons against FTIR measurements, which cannot be made ~~which is not possible~~ during the polar
151 night, Fig. 2 (top panel) presents the time series of daily IASI total HNO$_3$ columns co-located with MLS
152 measurements within 2.5°x2.5° grid boxes, averaged in the 70°S–90°S equivalent latitude band. In order
153 to account for the vertical sensitivity of IASI, the averaging kernels associated with each co-located IASI
154 retrieved profiles were applied to the MLS profiles~~considered~~ for this cross-comparison. The MLS VMR
155 profiles over the 215-1.5 hPa pressure range were first interpolated to the FORLI pressure grids ~~, then~~
156 ~~converted into column profiles. They were also~~ and extended down to the surface by ~~considering~~ using
157 the FORLI-HNO3 a priori profile, and then converted into partial columns. Similar variations in the
158 HNO$_3$ column are captured by the two instruments, with an excellent agreement in particular for the
159 timing of the strong HNO$_3$ depletion within the inner vortex core. Note that a similar good agreement
160 between the two satellite datasets is obtained in other latitude bands (see Fig. 2 bottom panel for the
161 50°S–70°S equivalent latitude band; the other bands are not shown).

163 Quality flags similar to those developed for O$_3$ in previous IASI studies (Wespes et al., 2017) were
164 applied a posteriori to exclude data (i) with a corresponding poor spectral fit (e.g. based on quality flags
165 rejecting biased or sloped residuals, fits with maximum number of iteration exceeded), (ii) with less
166 reliability (e.g. based on quality flags rejecting suspect averaging kernels, data with less sensitivity
167 characterized by a DOFS lower than 0.9) or (iii) with tropospheric cloud contamination (defined by a
168 fractional cloud cover ≥ 25 %). Note that the HNO$_3$ total column distributions illustrated in sections
169 below use the median as a statistical average since it is more robust against the outliers than the mean.

171 Temperature and potential vorticity (PV) fields are taken from the ECMWF ERA Interim Reanalysis
172 dataset, respectively at 50 hPa and at the potential temperature of 530 K (corresponding to ~20 km
173 altitude where the IASI sensitivity to HNO$_3$ is the highest during the Southern Hemisphere (S.H.) winter
174 (Ronsmans et al., 2016)). Because the HNO$_3$ uptake by PSCs starts within a few degrees ~~or slightly~~
175 below T_{NAT} (~195.7 K at 50 hPa (Hanson and Mauersberger, 1988)) depending on the meteorological
176 conditions (Pitts et al., 2013; Hoyle et al., 2013; Lambert et al., 2016; Pitts et al., 2018), a threshold
177 temperature of 195 K is considered in the sections below to identify regions of potential PSC
178 existence~~the PSCs-containing regions~~. The potential vorticity is used to delimit dynamically consistent
179 areas in the polar regions. In what follows, we use either the equivalent latitudes ("eqlat", calculated
180 from PV fields at 530 K) or the PV values to characterize the relationship between HNO$_3$ and
181 temperatures in the cold polar regions. Uncertainties in ERA-Interim temperatures will also be discussed
182 below.

184 **3 Annual cycle of HNO$_3$ vs temperatures**

186 Figure 3a shows the yearly HNO$_3$ cycle (solid lines, left axis) in the southernmost equivalent latitudes
187 (70° - 90° S), as measured by IASI over the whole study period ~~of measurements~~ (2008–2017). The total
188 HNO$_3$ variability in such equivalent latitudes has already been discussed in a previous IASI study
189 (Ronsmans et al., 2018), where the contribution of the PSCs ~~in~~to the HNO$_3$ variations was highlighted.
190 The temperature time series, taken at 50 hPa, is ~~here~~ represented as well (dashed lines, right axis). From
191 this figure, different regimes of HNO$_3$ total columns *vs* temperature can be observed throughout the year
192 and from one year to another. In particular, we define here three main regimes (R1, R2 and R3) ~~along~~
193 during the HNO$_3$/temperature annual cycle. The full cycle and the main regimes in the 70° - 90° S eqlat
194 region are further represented in Fig. 3b that shows a histogram of the HNO$_3$ total columns as a function
195 of temperature for the year 2011. Similar histograms are observed for the ten years of IASI

4

measurements (not shown). The red horizontal and vertical lines in Fig. 3a and Fig. 3b, respectively, represent the 195 K threshold temperature used to identify the onset of HNO$_3$ uptake by PSCs (see Section 2). The three identified regimes correspond to:

- R1 is defined by the maxima in the total HNO$_3$ abundances covering the months of April and May (~3×10^{16} molec.cm^{-2}~~, R1 in Figures 3a and b~~), when the 50 hPa temperature strongly decreases (from ~220 to ~195 K). These high HNO$_3$ levels result from low sunlight, preventing photodissociation, along with the heterogeneous hydrolysis of N$_2$O$_5$ to HNO$_3$ during autumn before the formation of polar stratospheric clouds (Keys et al., 1993; Santee et al., 1999; Urban et al., 2009; de Zafra and Smyshlyaev, 2001). This period also corresponds to the onset of the development~~deployment~~ of the southern polar vortex, which is characterized by strong diabatic descent with weak latitudinal mixing across its boundary, isolating polar HNO$_3$-rich air from lower--latitude~~inal~~ airmasses.

- R2, which extends from June to October, ~~is characterized by~~follows the onset of the strong decrease in HNO$_3$ total columns, which starts around mid-May in most years,~~at the beginning of June,~~ when the temperatures fall below 195 K, and is characterized by ~~followed by~~ a plateau of total HNO$_3$ minima. In this regime, average HNO$_3$ total columns are ~~the HNO$_3$ total columns average~~ below 2×10^{16} molec.cm^{-2} and the 50 hPa temperatures range mostly between 180 and 190 K.

- R3 starts in October when sunlight returns and the 50 hPa temperatures rise above 195 K. Despite 50 hPa temperatures increasing up to 240 K~~Despite the stratospheric warming with 50 hPa temperatures up to 240 K~~ in summer, the HNO$_3$ total columns stagnate at the R2 plateau levels (around 1.5×10^{16} molec.cm^{-2}). This regime likely reflects the photolysis of NO$_3$ and HNO$_3$ itself (Ronsmans et al., 2018) as well as the permanent denitrification of the mid-stratosphere, caused by sedimentation of PSCs~~by the PSCs sedimentation~~. The likely renitrification of the lowermost stratosphere (e.g. Braun et al., 2019; Lambert et al., 2012), where the HNO$_3$ concentrations and the IASI sensitivity to HNO$_3$ are lower (Ronsmans et al., 2016), cannot~~can hardly~~ be inferred from the IASI total column measurements. The plateau lasts until approximately February, when~~re~~ HNO$_3$ total column slowly starts increasing, reaching the April-May maximum in R1.

As illustrated in Fig. 3a, the three regimes are observed each year with, however, some interannual variations. For instance, the sudden stratospheric warming (SSW) that occur**red**~~s~~ in 2010 (see the temperature time series at 20 hPa for the year 2010; green dotted line) yielded higher HNO$_3$ total columns (see green solid line in July ~~and August~~ - September) (de Laat and van Weele, 2011; Klekociuk et al., 2011; WMO, 2014; Ronsmans et al., 2018).

Figure 3c shows the evolution of the relationship between the daily averaged HNO$_3$ (calculated from a 7-day moving average) with the highest occurrence (in bins of 0.1×10^{16} molec.cm^{-2} and of 2K) and the 50 hPa temperature, over the 10 years of IASI. The red vertical line represents the 195 K threshold temperature. Figure 3c clearly illustrates the slow increase in HNO$_3$ columns as the temperatures decrease (February to May, i.e. R3 to R1), the strong and rapid HNO$_3$ depletion occurring in June (R2), and the plateau of low HNO$_3$ abundances in winter and spring (from July ~~August~~ to November; R2 to R3). Figure 3c also highlights ~~the~~a large interannual variability in total HNO$_3$~~, which is found to be the largest~~ in R3, while the strong depletion in HNO$_3$ in R2 ~~and~~ ~~shows a strong consistency in the~~is consistent ~~onset of the depletion~~ every ~~between each~~ year (beginning of June when the temperatures fall below 195 K as indicated by the red vertical line). Given that PSC formation spans a large range of altitudes ~~Given the span of PSCs formation over a large range of altitudes~~ (typically between 10 and 30

5

km) (Höpfner et al., ~~150~~ 2006, 2009; Spang et al., 2018; Pitts et al., 2018) and that IASI has maximum sensitivity to ~~that of maximum IASI sensitivity to~~ HNO_3 around 50 hPa (Hurtmans et al., 2012; Ronsmans et al., 2016), the temperatures at two other pressure levels, namely 70 and 30 hPa (i.e. ~15 and ~25 km), have also been tested to investigate the relationship between HNO_3 and temperature in the low and mid-stratosphere. The results (not shown here) exhibit a similar HNO_3-temperature behavior at the different levels with, as expected, lower and l~~arger~~higher temperatures in R2, respectively, at 30 hPa ~~(down to ~180 K)~~ and at 70 hPa (temperatures down to ~180 K at 30 hPa and down to ~185 K at 70 hPa, as compared to temperatures down to ~182 K at 50 hPa, are observed), but still below the NAT formation threshold at these pressure levels (T_{NAT} ~193 K at 30 hPa and ~197 K at 70 hPa) (Lambert et al., 2016). Therefore, the altitude range of maximum IASI sensitivity to HNO_3 (see Section 2) is characterized by temperatures that are below the NAT formation threshold at these pressure levels, enabling ~~the~~ PSC~~s~~ formation and the denitrification process. Furthermore, the consistency between the 195 K threshold temperature taken at 50 hPa and the onset of the strong total HNO_3 depletion seen in IASI data (see Fig. 3a ~~and Fig. 3c~~) is in agreement with the largest NAT area that starts to develop in June around 20 km (Spang et al., 2018), which justifies the use of the 195 K temperature at that single representative level in this study.

4 Onset of HNO_3 depletion and drop temperature detection

To identify the spatial and temporal variability of the onset of the depletion phase, the daily time evolution of HNO_3 during the first 10 years of IASI measurements and the temperatures at 50 hPa are explored. In particular, the second derivative of HNO_3 total column with respect to time is calculated to detect the strongest rate of decrease seen in the HNO_3 time series and to identify its associated day and 50 hPa temperature.

4.1 HNO_3 vs temperature time series

Figure 4 shows the time series of the second derivative of HNO_3 total column with respect to time (blue) and of the temperature (red) averaged in the area~~s~~ of potential vorticity at the potential temperature of 530 K smaller than -10×10^{-5} $K.m^2.kg^{-1}.s^{-1}$ to encompass the region~~s~~ inside the inner polar vortex where the temperatures are the coldest and ~~the total HNO_3 depletion occurs~~ the largest depletion of total HNO_3 occurs (Ronsmans et al., 2018). The use of that PV threshold value explains the gaps in the time series during the summer when the PV does not reach such low levels, while the time series averaged in the 70°- 90° S Eqlat band (dashed blue for the second derivative of HNO_3 and grey for the temperature) covers the full year. Note that the HNO_3 time series has been smoothed with a simple spline data interpolation function to avoid gaps in order to calculate the second derivative of HNO_3 total column with respect to time as the daily second-difference in HNO_3 total column~~s~~. The horizontal red line shows the 195 K threshold.

As already illustrated in Fig. 3a and Fig. 3c, the strongest rate of HNO_3 depletion (i.e. the second derivative minimum) is found ~~around the 195 K threshold temperature~~ around the time that temperatures drop below the 195 K threshold, ~~within some days~~ within a few days to a few weeks (4 to 23 days) after total HNO_3 reaches its maximum, i.e. between the 12~~1~~th of May (2013) and the 8th of June (2009). ~~Except for the year 2014, t~~The 50 hPa drop temperatures, i.e. the temperature associated with the strongest HNO_3 depletion detected from IASI, are detected between 189.2 K and 198.6 K with an exception for the year 2014 which shows a drop temperature of 202.8 K. On average over the 10 years of studied IASI measurements, a 50 hPa drop temperature of ~~(~~194.2~~1~~ K ± ~~2~~3.8 K (~~−~~1σ standard deviation) is found. ~~ on average over the 10 years, excluding 2014 that stands out with a drop temperature of 202.8 K)~~. Knowing that T_{NAT} can be higher or lower depending on the atmospheric

conditions and that NAT starts to nucleate from ~2–4 K below T_{NAT} (Pitts et al., 2011; Hoyle et al., 2013; Lambert et al., 2016), the results here tend to demonstrate the consistency between the 50 hPa drop temperature, i.e. the temperature associated with the strongest HNO₃ depletion detected from IASI, and the PSCs formation existence temperature in that altitude region. Note that the range observed in the 50 hPa drop temperature could reflect the preponderance by one type variations in the preponderance of one type of PSCs over another from one year to the next. The results further justify the use of the single 50 hPa level for characterizing and investigating the onset of HNO₃ depletion from IASI. Nevertheless, given the range of maximum IASI sensitivity to HNO₃ around 50 hPa, typically between 70 and 30 hPa (Ronsmans et al., 2016), the drop temperatures are also calculated at these two other pressure levels (not shown here) in order to estimate the uncertainty of the calculated drop temperature defined in this study at 50 hPa. The 30 hPa and 70 hPa drop temperatures range respectively over 185.7 K –194.9 K and over 194.8 K – 203.7 K, with an average of 192.0 ± 2.9 K and 198.0 ± 3.2 K (1σ standard deviation) over the ten years of IASI. The average values at 30 hPa and 70 hPa fall within the 1σ standard deviation associated with the average drop temperature at 50 hPa. It is also worth noting the agreement between the drop temperatures and the NAT formation threshold at these two pressure levels (T_{NAT} ~ 193 K at 30 hPa and ~197 K at 70 hPa) (Lambert et al., 2016). Finally, it should be noted that, because the size, shape or location of the vortex vary slightly over the altitude range to which IASI is sensitive (from ~30 to ~70 hPa during the polar night), the use of a single potential temperature surface for the calculation of drop temperatures could introduce some uncertainties into the results. However, several tests suggest that these variations of the vortex are overall minor and, hence, could only have limited influence on the delimitation of the inner polar vortex (delimited by a PV value of -10×10^{-5} K.m².kg⁻¹.s⁻¹ at 530 K) and on the detection of the average drop temperature inside that region.

Figures 5a and b show the climatological zonal distribution of HNO₃ total columns and of the temperature at 50 hPa, respectively, spanning the 55° S - 90° S geographic latitude band over the whole IASI period, with, superimposed, three isocontour levels of potential vorticity (-10, -8 and -5×10⁻⁵ K.m².kg⁻¹.s⁻¹ in blue, cyan and black, respectively) and the isocontours for the 195 K temperature (pink) and for the averaged 194.2 K drop temperature (purple) at 50 hPa one isocontour for the 50 hPa temperature. They further illustrate the relationship between the IASI total HNO₃ columns and the 50 hPa temperatures. The average PV isocontour of -10×10⁻⁵ K.m².kg⁻¹.s⁻¹ is clearly shown to separate well the region of strong depletion in total HNO₃ according to the latitude and the time. The red vertical dashed lines indicates the average date for the 50 hPa average drop temperatures calculated in the area of PV≤ -10×10⁻⁵ K.m².kg⁻¹.s⁻¹ (194.2 ± 3.8 K; see Fig. 4) over the IASI period. It shows that the strongest rate in of HNO₃ depletion occurs on average end of May a few days before June, a few days after the temperature decreases below 195 K. The delay of some days between the maximum in total HNO₃ and the start of the depletion (see Fig. 4) is also visible in Fig. 5a. For the purpose of the illustrations, The the yearly zonally averaged time series over the ten years of IASI can be found in Fig. 6; it shows the reproducibility of the edge of the collar HNO₃ region and of the region of the strong HNO₃ depletion, respectively delimited by the PV isocontours of -5×10⁻⁵ K.m².kg⁻¹.s⁻¹ and of -10×10⁻⁵ K.m².kg⁻¹.s⁻¹ at 50 hPa530 K, measured by IASI from year to year, as well as the reproducibility of the NAT threshold temperature region that encompasses the inner vortex core. Except for the year 2009, the dates for the strongest rate of HNO₃ depletion matches those for the onset of decreasing temperatures below 195 K.

4.2 Distribution of drop temperatures

To explore the capability of IASI to monitor the onset of HNO₃ depletion at a large scale from year to year, figure 7 shows the spatial distribution of the 50 hPa drop temperatures (based on the second derivative minima of total HNO₃ averaged in 1°×1° grid cells) inside a region delimited by a PV value of -8×10⁻⁵ K.m².kg⁻¹.s⁻¹, for each year of the IASI period in order to investigate a region a bit larger than

343 that of the strong depletion in total HNO$_3$ encircled by . The green contour represents the PV isocontour
344 of -10×10^{-5} K.m^2.kg^{-1}.s^{-1}, averaged over the period 10 May – 15 July period for each year, which delimits
345 our region of interest (in green). The isocontour of -10×10^{-5} K.m^2.kg^{-1}.s^{-1} for the minimum PV (in cyan)
346 encountered at 530 K over the 10 May to 15 July period for each year, as well as Tthe isocontours of
347 195 K for the average temperatures and the minimum temperatures, as well as the isocontour of -10×10^{-}
348 ^{5} K.m^2.kg^{-1}.s^{-1} for the minimum PV encountered at 50 hPa over the 10 May to 15 July period, are also
349 represented. The calculated drop temperatures corresponding to the onset of HNO$_3$ depletion inside the
350 averaged PV isocontour are found to vary between ~180 and ~210 K and the corresponding dates range
351 between ~mid-May and mid-July (not shown here). The year 2014 that shows the highest average drop
352 temperature in Figure 4 is characterized by the highest drop temperatures above the eastern Antarctic.
353 Note, however, that the high extremes in the drop temperature, which are found in some casesmainly
354 found above the eastern Antarctica, should be considered with caution: they correspond to specific
355 regions above ice surfaces with emissivity features that are known to yield errors in the IASI retrievals
356 (Hurtmans et al., 2012; Ronsmans et al., 2016). Indeed, bright land surfaces such as ice might in some
357 cases lead to poor HNO$_3$ retrievals. Although wavenumber-dependent surface emissivity atlases are used
358 in FORLI (Hurtmans et al., 2012), this parameter remains critical and causes poorer retrievals that, in
359 some instances, pass through the series of quality filters and could affect the drop temperature
360 calculation.
361
362 The averaged isocontour of 195 K encircles fairly well the area of HNO$_3$ drop temperatures lower than
363 195 K (typically from ~187 K to ~195 K), which means that the bins inside that area characterizeinclude
364 airmasses that experience the NAT threshold temperature during a long time over the 10 May – 15 July
365 period. That area encompasses the inner vortex core (delimited by the isocontour of -10×10^{-5} K.m^2.kg^{-}
366 ^{1}.s^{-1} for the PV averaged over the 10 May – 15 July period) and shows pronounced minima (lower than
367 -0.5×10^{14} molec.cm^{-2}.d^{-2}) in the second derivative of the HNO$_3$ total column with respect to time (not
368 shown here), which indicate a strong and rapid HNO$_3$ depletion. The area enclosed between the two
369 isocontours of 195 K for the temperatures, the averaged one and the one for the minimum temperatures,
370 shows generally higher drop temperatures and weakest minima (larger than -0.5×10^{14} molec.cm^{-2}.d^{-2}) in
371 the second derivative of the HNO$_3$ total column (not shown). That area is also typically enclosed by the
372 isocontour of -10×10^{-5} K.m^2.kg^{-1}.s^{-1} for the minimum PV, meaning that the bins inside correspond, at
373 least for one day over the 10 May – 15 July period, to airmasses located at the inner edge of the vortex
374 and characterized by temperature lower than the NAT threshold temperature. The fact that the weakest
375 minima in the second derivative of total HNO$_3$ (not shown) are observed in that area indicatesThe
376 weakest minima in the second derivative of total HNO$_3$ (not shown) observed in that area indicate a
377 weak and slow HNO$_3$ depletion and might be explained by a short period of the NAT threshold
378 temperature experienced at the inner edge of the vortex. It could also reflect a mixing with strong reflect
379 mixing with strongly HNO$_3$-depleted and colder airmasses from the inner vortex core. The mMixing
380 with these already depleted airmasses could also explained the higher drop temperatures detected in
381 those bins. These sometimes unrealistic high drop temperatures are generally detected later (after the
382 strong HNO$_3$ depletion occurs in the inner vortex core, i.e. after the 10 May – 15 July period considered
383 here – not shown), which supports the transport, in those bins, of earlier HNO$_3$-depleted airmasses and
384 the likely mixing at the edge of the vortex. Note, however, that previous studies have shown a generally
385 weak mixing in the Antarctic between the edge region and the vortex core (e.g. Roscoe et al., JGR 2012).
386 Finally, these spatial variations might also partly reflect some uncertainty into the drop temperature
387 calculation, introduced by the use of temperature at a single pressure level (50 hPa) and of the PV on a
388 single potential temperature surface (530 K), despite the range of the sensitivity of the IASI total column
389 measurements to changes in HNO3 profiles (from ~30 to ~70 hPa during the polar night). the range of
390 maximum sensitivity of IASI to HNO$_3$,. It should be note that biases in the ECMWF ERA Interim
391 temperatures used in this work, while biases in ECMWF reanalysis are too small for explainingto explain

the ~~spatial variation~~large range of ~~in~~ drop temperatures calculated here. Indeed, Lambert and Santee (2018) found a small warm bias, with median differences around 0.5 K, reaching 0–0.25 K in the southernmost regions of the globe at ~68–21 hPa where PSCs form, through comparisons with the COSMIC data. ~~Thanks to the assimilation of an advanced Tiros Operational Vertical Sounder (ATOVS) around 1998–2000 in reanalyses, to the better coverage of satellite instruments and to the use of global navigation satellite system (GNSS) radio occultation (RO) (Schreiner et al., 2007; Wang et al., 2007; Lambert and Santee, 2018; Lawrence et al., 2018), the uncertainties have been vastly reduced. Comparisons of the ECMWF ERA-Interim dataset used in this work with the COSMIC data (Lambert and Santee, 2018) found a small warm bias, with median differences around 0.5 K, reaching 0–0.25 K in the southernmost regions of the globe at ~68–21 hPa where PSCs form.~~

Except above some parts of Antarctica which are prone to larger retrieval errors and where unrealistic high drop temperatures are found, the overall range in the ~~drop~~ 50 hPa drop temperature for total HNO_3 inside the isocontour for the averaged temperature of 195 K~~,~~ typically extends from ~187 K to ~195 K, which falls within the range of PSC~~s~~ nucleation temperature at 50 hPa: from slightly below T_{NAT} to around 3-4 K below the ice frost point - T_{ice} - depending on atmospheric conditions, on TTE and ~~on the type of formation mechanisms~~ on the specific formation mechanism (i.e., the type of PSC developing) (Pitts et al., 2011; Peter and Grooß, 2012; Hoyle et al., 2013). This underlines well the benefit of the excellent spatial and temporal coverage of IASI, which allows the rapid and critical depletion phase to be captured in detail ~~that allows capturing the rapid and critical depletion phase~~ over a large scale.

5 Conclusions

In this paper, we have explored the added value of the dense HNO_3 total column~~s~~ dataset provided by the IASI/Metop-A satellite over a full decade (2008–2017) for monitoring the stratospheric depletion phase that occurs each year in the S.H. and for investigating its relationship to the NAT formation temperature. To that end, we focused on and delimited the coldest polar region of the S.H. using a specific PV value at 530 K (~50 hPa, PV of -10×10^{-5} $K.m^2.kg^{-1}.s^{-1}$) and stratospheric temperatures at 50 hPa, taken from the ECMWF ERA Interim reanalysis. That single representative pressure level has been considered in this study given the maximum sensitivity of IASI to HNO_3 around that level, which lies in the range where ~~over a range where~~ the PSCs formation/denitrification process~~es~~ occur.

The annual cycle of total HNO_3, as observed from IASI, has first been characterized according to the temperature evolution. Three ~~various~~ regimes (R1 to R3) in the total HNO_3 - 50 hPa temperature relationship were highlighted from the time series over the S.H. polar region ~~and described along the cycle~~: R1 is defined ~~at play~~ during April and May and characterized by a rapid decrease in 50 hPa temperatures while HNO_3 accumulates in the poles; R2, from June to September, ~~shows~~follows the onset of the depletion that starts around mid-May in most years when the 50 hPa temperatures fall below 195 K (considered here as the onset of PSC~~s~~ nucleation phase at that level), with a strong consistency ~~between each year~~from year to year; R3, defined from ~~November~~October ~~until~~through March when total HNO_3 remains at low R2 plateau levels, despite the return of sunlight and heat, characterizes the strong denitrification of the stratosphere, likely due to PSC~~s~~ sedimentation ~~at~~to lower levels where the IASI sensitivity is low. For each year over the IASI period, the use of the second derivative of the HNO_3 column versus time was then found to be particularly valuable to detect the onset of the HNO_3 condensation ~~in~~to PSCs. It is captured, on average from IASI, a few days before June with a delay of 4–23 days after the maximum in total HNO_3. ~~Except for the year 2014, t~~The corresponding temperatures ('drop temperatures') were detected between 189.2 K and ~~198.6~~202.8 K (194.~~1~~2 ± ~~2~~3.8 on average over the 10 years~~, excluding the year 2014 that shows a drop temperature of 202.8 K~~), which tends to

9

demonstrate~~d~~ the good consistency between the 50 hPa drop temperature and the PSC~~s~~ formation temperatures in that altitude region. Finally, the annual and spatial variability (within $1° \times 1°$) in the drop temperature was further explored from IASI total HNO_3. Inside the isocontours of 195 K for the average temperatures and of -10×10^{-5} K.m^2.kg^{-1}.s^{-1} for the averaged PV at ~~50 hPa~~530 K, the drop temperatures are detected between ~mid-May and mid-July, typically range between ~187 K to ~195 K and are associated with the ~~highest~~lowest minima (lower than -0.5×10^{14} molec.cm^{-2}.d^{-2}) in the second derivative of the HNO_3 total column with respect to time, indicating a strong and rapid HNO_3 depletion. Except for extreme drop temperatures (~210 K) that were found ~~from year to year~~in some years above eastern Antarctica and suspected to result from unfiltered poor quality retrievals in case of emissivity issues above ice, the range of drop temperatures is interestingly found to be in line with the PSC~~s~~ nucleation temperature that is known, from previous studies, to strongly depend on a series of~~a~~ factors (e.g. meteorological conditions, HNO_3 vapour pressure, temperature threshold exposure, presence of meteoritic dust). At the edge of the vortex, considering the isocontours of 195 K for the minimum temperatures or of -10×10^{-5} K.kg^{-1}.s^{-1} for the minimum PV, higher and later drop temperatures along with weakest minima in the second derivative of the HNO_3 total column with respect to time, indicating a slow HNO_3 depletion, are found. ~~It~~These likely results from a short temperature threshold exposure or ~~a~~ mixing with already depleted airmasses from the inner vortex core. The results of this study highlight the ability of IASI to measure the variations in total HNO_3 and, in particular, to capture and monitor the rapid depletion phase over the whole Antarctic ~~polar~~ regions.

We show in this study that the IASI dataset allows ~~capturing~~ the variability of stratospheric HNO_3 throughout the year (including the polar night) in the Antarctic to be captured. In that respect, it offers ~~a new~~ observational means to monitor the relation of HNO_3 to temperature and the related formation of PSCs. Despite the limited vertical resolution of IASI which does not allow ~~to investigate~~ investigation of the HNO_3 uptake by the different types of PSCs during their formation and growth along the vertical profile, the HNO_3 total column measurements from IASI constitute an important new dataset for exploring the strong polar depletion over the whole stratosphere. This is particularly relevant considering the mission continuity, which will span several decades with the planned follow-on missions. Indeed, thanks to the three successive instruments (IASI-A launched in 2006 and still operating, IASI-B in 2012, and IASI-C in 2018) that demonstrate an excellent stability of the Level-1 radiances, the measurements will soon provide an unprecedented long-term dataset of HNO_3 total columns. Further work could also make use of this unique data set to investigate the relation between HNO_3, O_3, and meteorology in the changing climate.

Data availability
The IASI HNO_3 data processed with FORLI-HNO_3 v0151001 are available upon request to the corresponding author.

Author contributions
G.R. performed the analysis, wrote the manuscript and prepared the figures. C.W. and L.C. contributed to the analysis. C.W., S.S., P.-F. C. and L.C. contributed to the interpretation of the results. D.H. was responsible for the retrieval algorithm development and the processing of the IASI HNO_3 dataset. All authors contributed to the writing of the text and reviewed the manuscript.

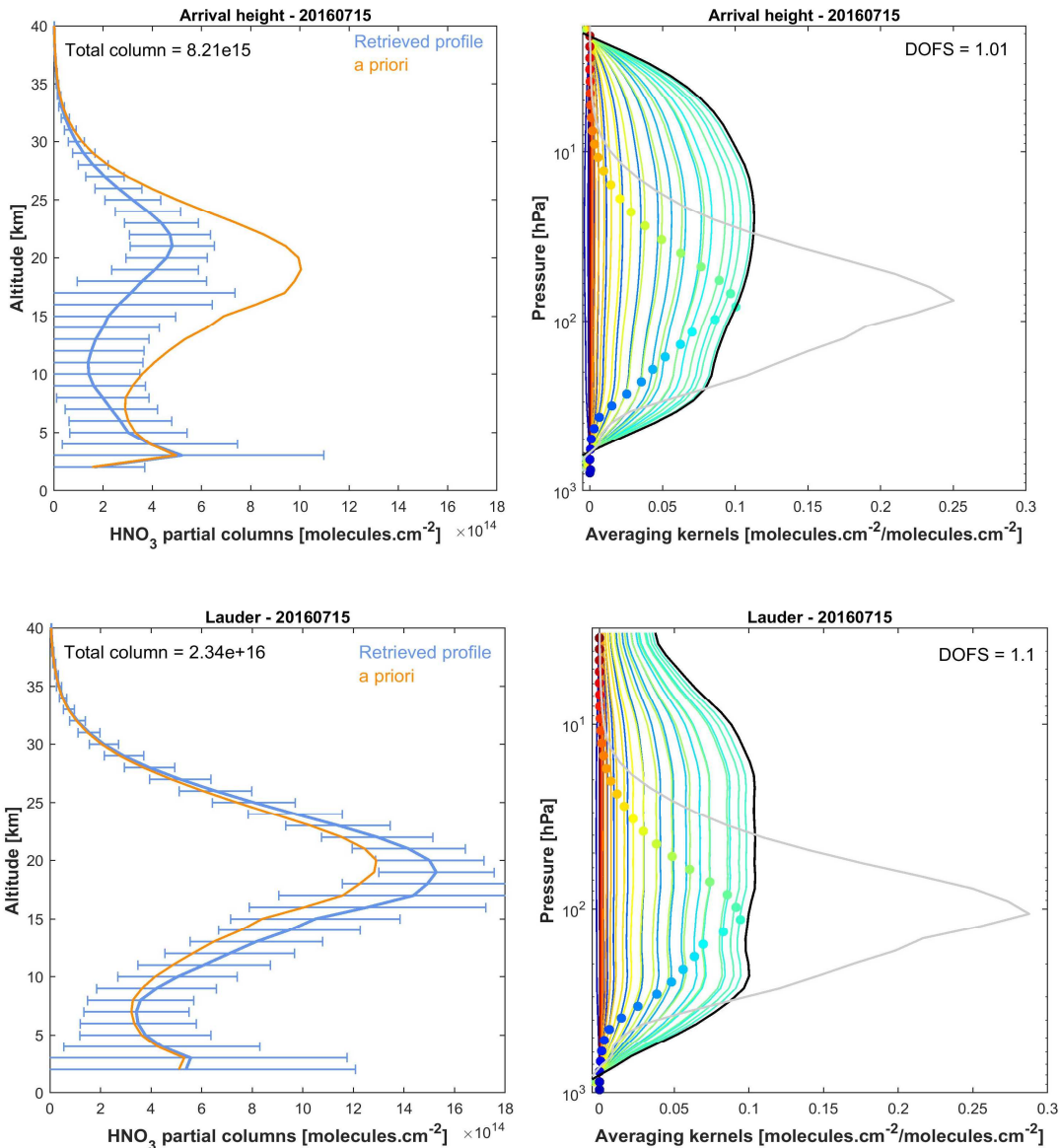**Competing interests**
The authors declare no competing interests.

499
500
501
502
503
504
505
506
507
508
509
510
511
512
513
514
515
516
517
518
519
520
521
522
523
524
525
526
527
528
529
530
531
532
533
534
535
536
537

Figure captions

544   Figure 1. Examples of IASI HNO_3 vertical profiles (in molec.cm^{-2}) with corresponding averaging kernels (in
545   molec.cm^{-2}/molec.cm^{-2}; colored lines, with the altitude of each kernel represented by the colored dots)
546   along with the total column averaging kernels (black) and the sensitivity profiles (grey) (divided by 10) above
547   Arrival Heights (77.49°S, 166.39°E, top panels) and Lauder (45.03°S, 169.40°E; bottom panels). The error bars
548   associated with the HNO_3 vertical profile represent the total retrieval error. The a priori profile is also represented.
549   The total column and the DOFS values are indicated.

550

12
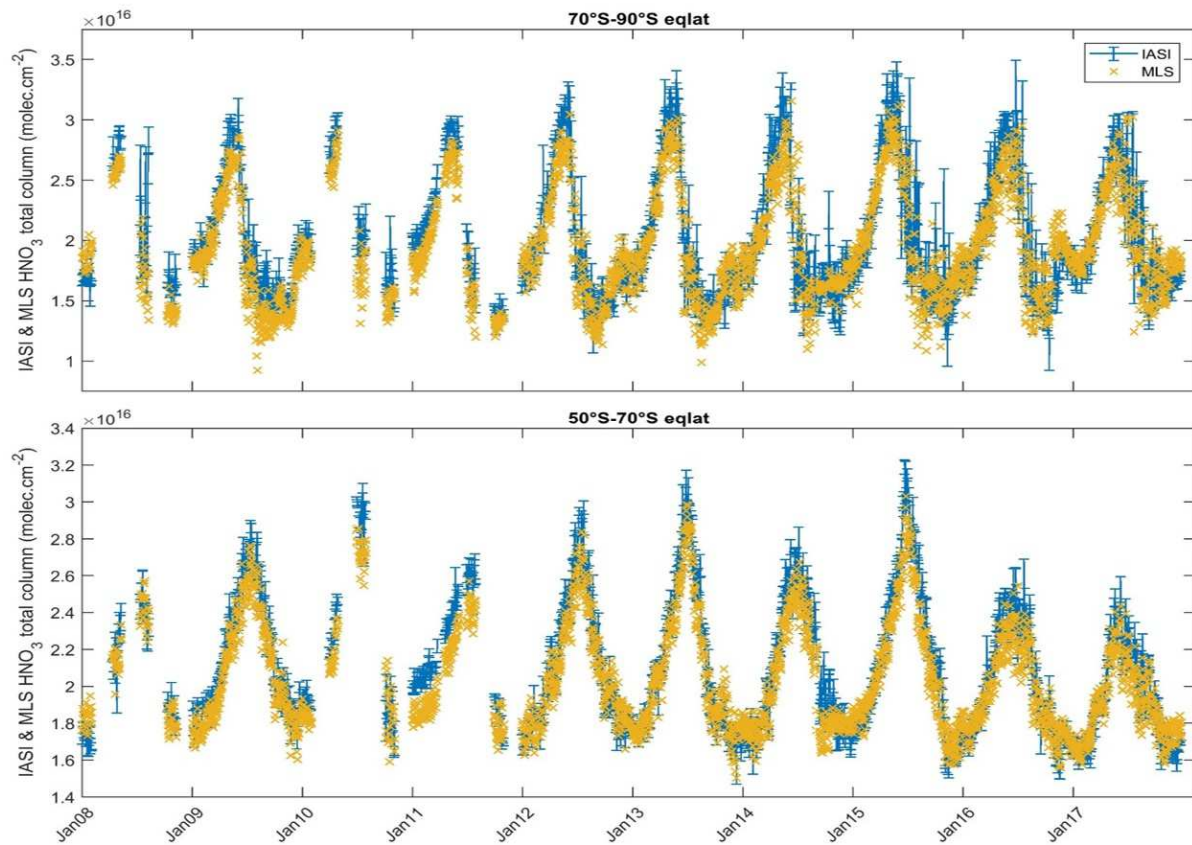
Figure 2. Time series of daily IASI total HNO₃ column (blue) co-located with MLS and of MLS total HNO₃ columns (orange) within 2.5°x2.5° grid boxes, averaged in the 70°S–90°S (top panel) and, the 50°S–70°S (~~middle~~bottom panel) ~~and the 30°S–50°S (bottom panel)~~ equivalent latitude bands. Note that the MLS total column estimates were obtained by extending the MLS partial stratospheric column values using the FORLI-HNO₃ a priori information (see text for details). The error bars (blue) represent~~s~~ 3σ, where σ is the standard deviation around the IASI HNO₃ daily average.

13
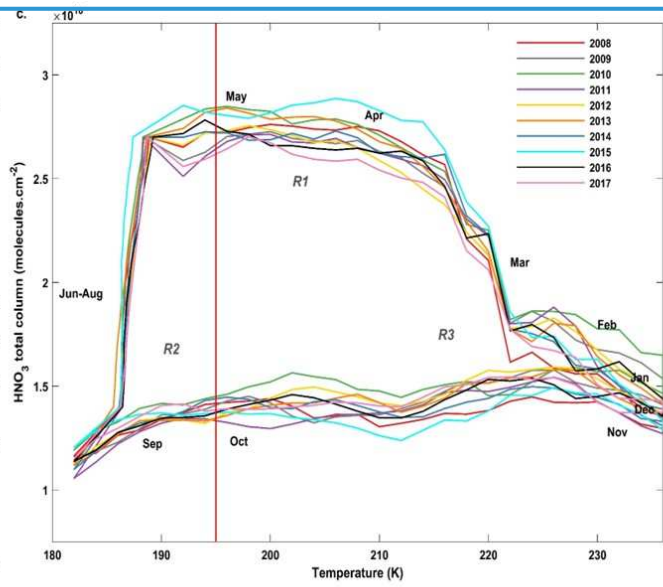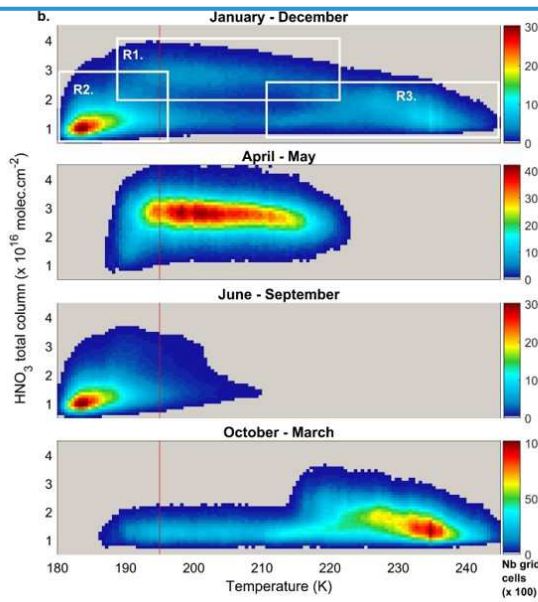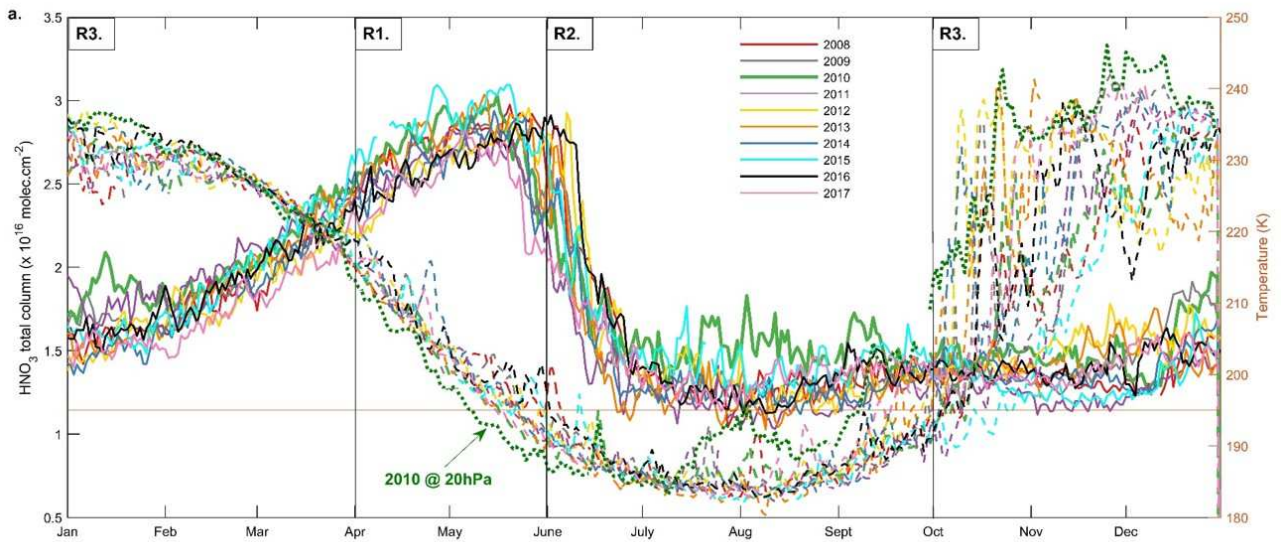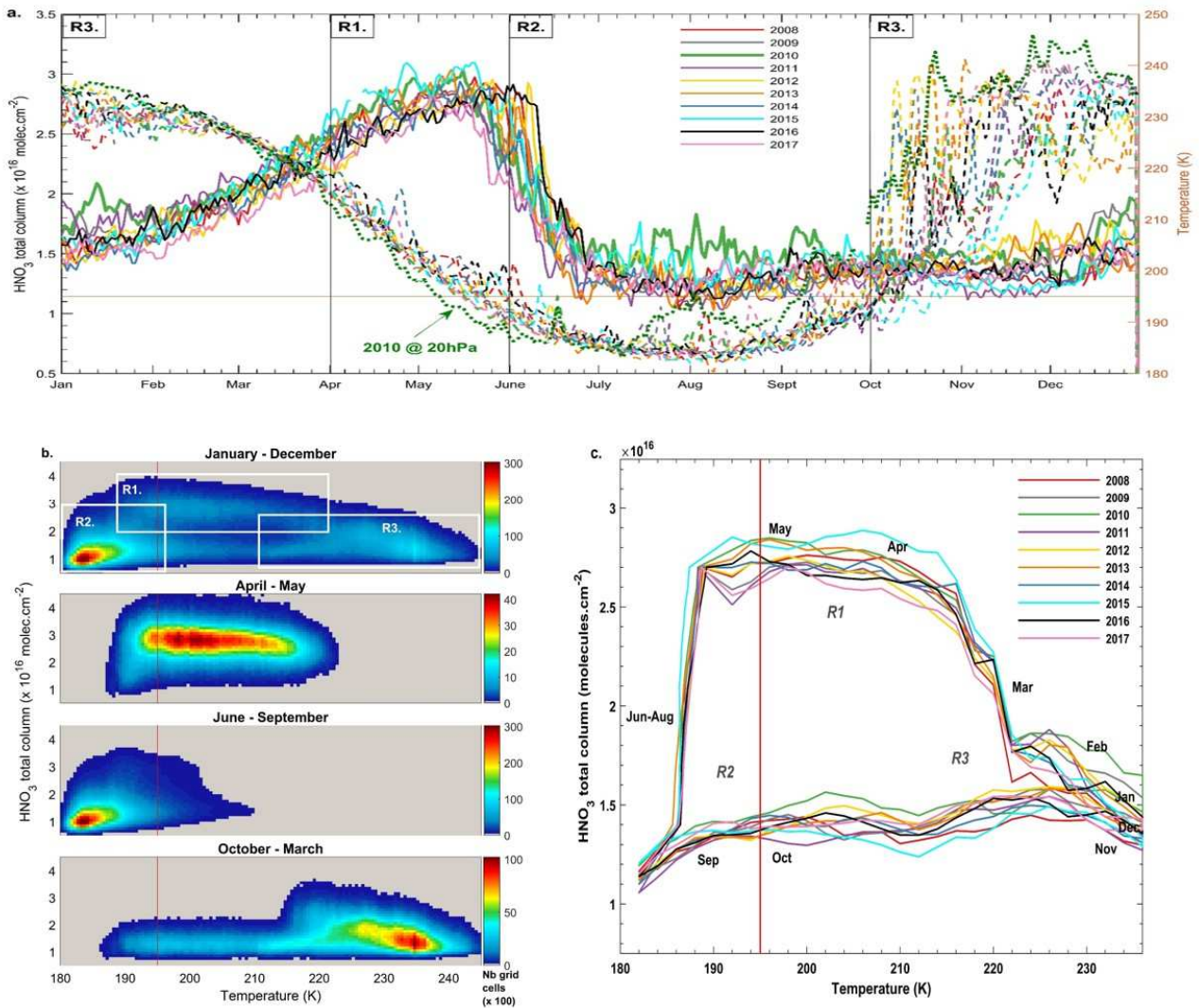
Figure 3. (a) Time series of daily averaged HNO₃ total columns (solid lines) and temperatures taken at 50 hPa (dashed lines) in the 70° - 90° S equivalent latitude band, for the years 2008 – 2017. The green dotted line represents the temperatures at 20 hPa for the year 2010. (b) HNO₃ total columns versus temperatures (at 50 hPa) histogram for the whole year (top) and for the 3 defined regimes (R1 - R3) separated in (a) for the year 2011. The colors refer to the number of gridded measurements in each cell. (c) Evolution of daily averaged HNO₃ total columns with the highest occurrence (in bins of 0.1×10¹⁶ molec.cm⁻² and 2 K) as a function of the 50 hPa temperature for the years 2008 – 2017. The red horizontal or vertical lines represent the 195 K threshold temperature.
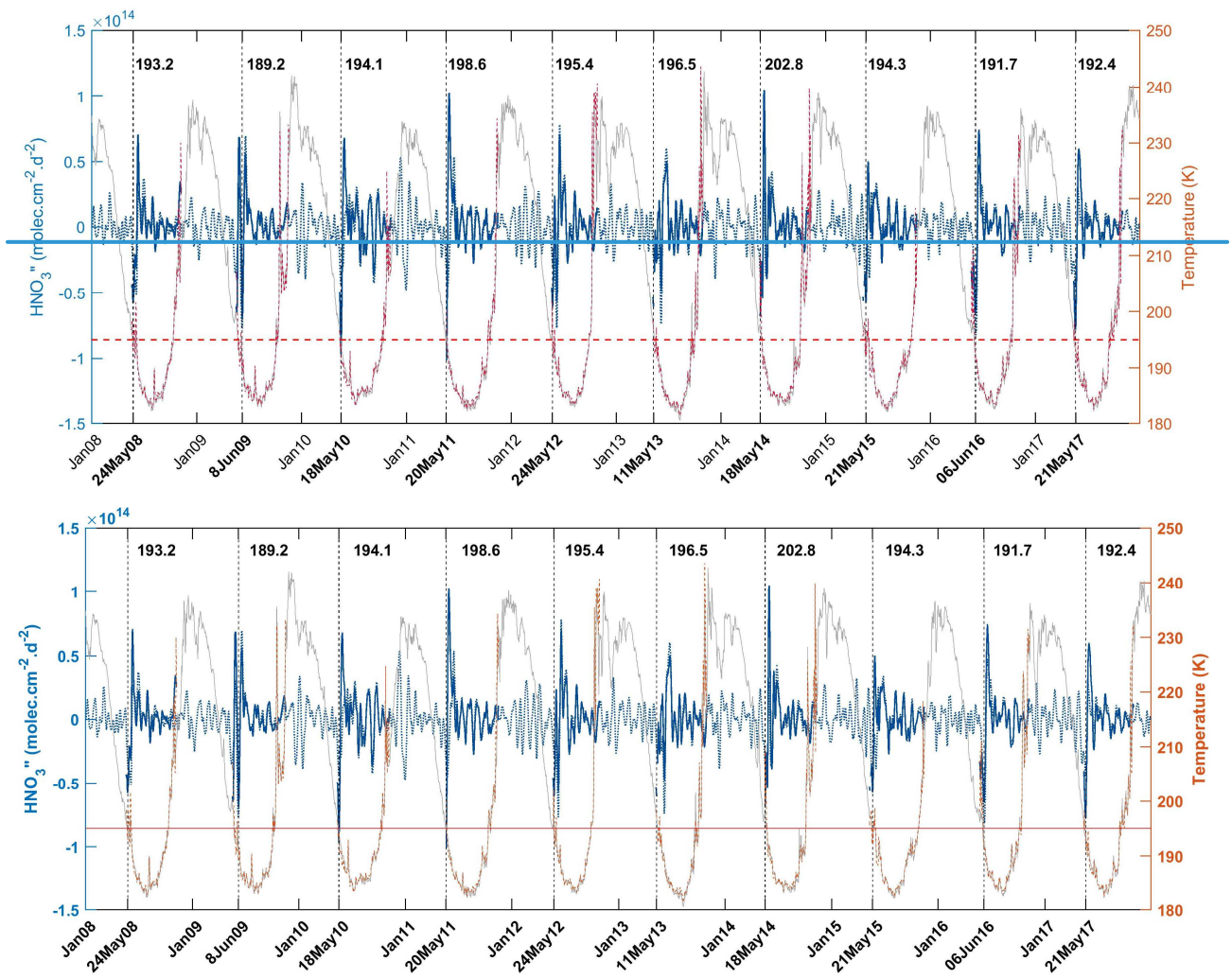
15

**Figure 4.** Time series of total HNO$_3$ second derivative (blue, left y-axis) and of the 50 hPa temperature (red, right y-axis), in the region of potential vorticity at 530 K lower than -10×10^{-5} K.m^2.kg^{-1}.s^{-1}. The red horizontal line corresponds to the 195 K temperature. The vertical dashed lines indicate the second derivative minimum in HNO$_3$ for each year. The corresponding dates (in bold, on the x-axis) and temperatures are also indicated. The time series of total HNO$_3$ second derivative (dashed blue) and of temperature (grey) in the 70° – 90° S Eqlat band are also represented.

16
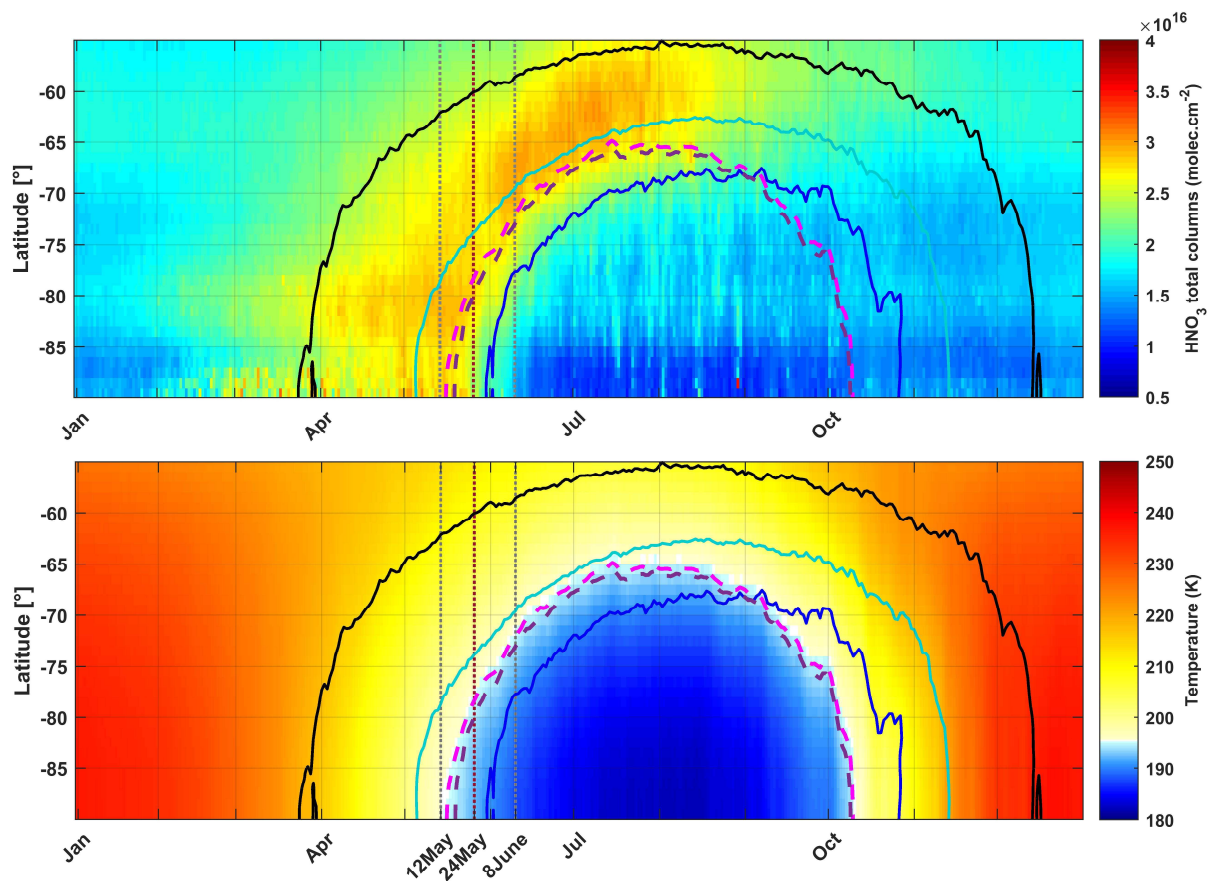
Figure 5. Zonal distributions of (a) HNO₃ total columns (in molec.cm⁻²) from IASI and (b) temperatures at 50 hPa from ERA Interim (in K) ~~between~~in the 55° S to 90° S geographical latitude band ~~south~~ and averaged over the years 2008 – 2017. Three isocontours for PV of -5 (black), -8 (cyan) and -10 (blue) (×10⁻⁵ K.m².kg⁻¹.s⁻¹) at 530 K, the isocontours for the 195 K temperature (pink) and for the averaged 194.2 K drop temperature (purple) at 50 hPa are superimposed. The vertical grey dashed lines mark the earliest and latest dates for the drop temperature in the 10-year IASI record ~~encompass the period of the second derivative minima~~ and the red one indicates the average date for the drop temperatures calculated in the area delimited by a -10×10⁻⁵ K.m².kg⁻¹.s⁻¹ PV contour.

17
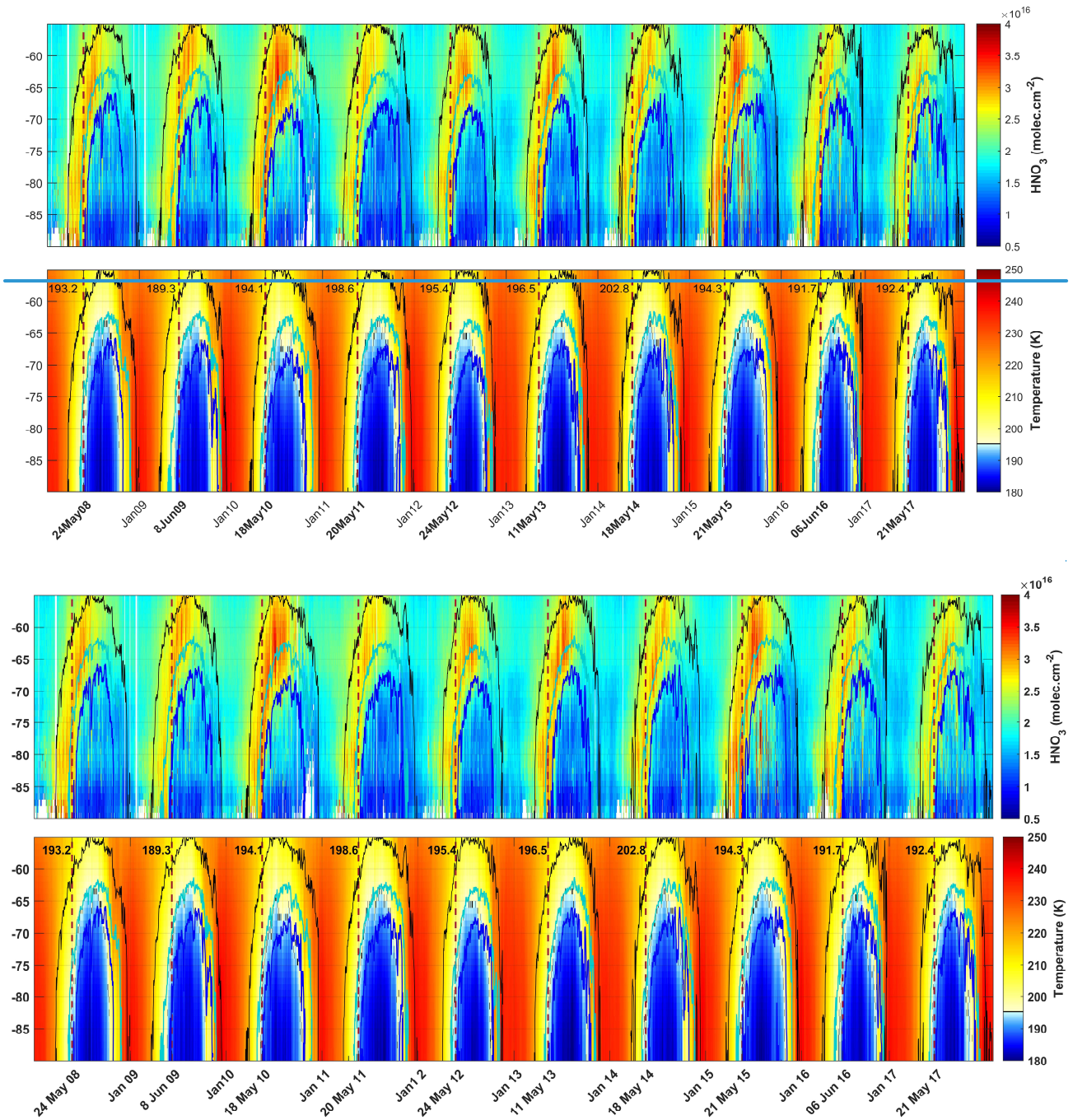
Figure 6. Zonally averaged distributions of (top) HNO_3 total columns (in molec.cm^{-2}) from IASI and (bottom) temperatures at 50 hPa from ERA Interim (in K). The geographical latitude range is from 55° to 90° south and the isocontours are PVs of -5 (black), -8 (cyan) and -10 (blue) ($\times$ 10^{-5} K.m^2.kg^{-1}.s^{-1} at 530 K). The vertical red dashed lines correspond to the second derivative minima each year in the area delimited by a -10×10^{-5} K.m^2.kg^{-1}.s^{-1} PV contour.
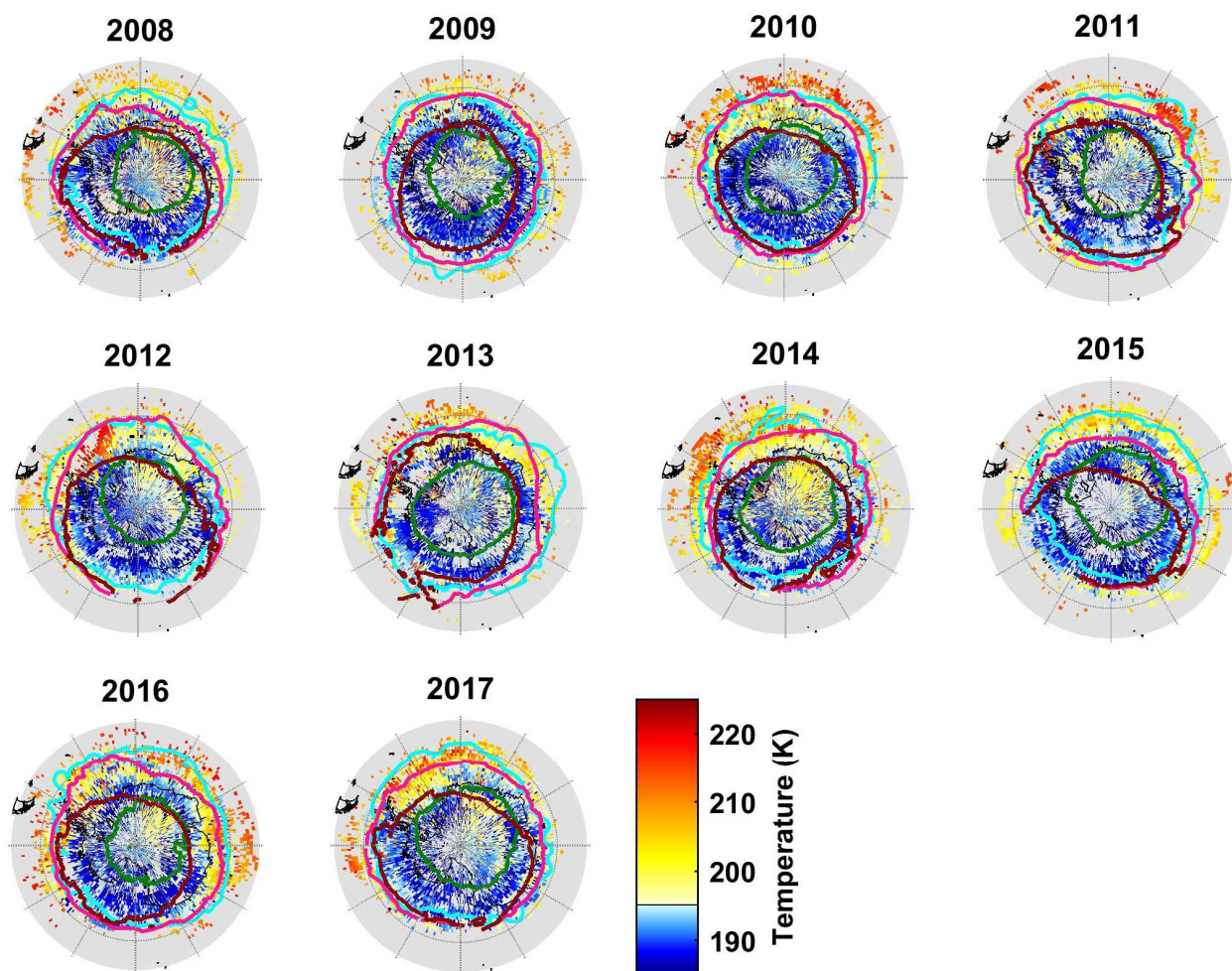
18

Figure 7. Spatial distribution (1°×1°) of the drop temperature at 50 hPa (K) (calculated from the total HNO_3 second derivative minima) for each year of IASI (2008–2017), in a region defined by a PV of -8×10^{-5} $K.m^2.kg^{-1}.s^{-1}$. The isocontours of -10×10^{-5} $K.m^2.kg^{-1}.s^{-1}$ at 530 K for the averaged PV (in green) and the minimum PV (in cyan) encountered over the period 10 May –15 July~~ne~~ for each year and the isocontours of 195 K at 50 hPa for the averaged (in red) and the minimum (in pink) temperatures over the same period are represented.

19

References

Braun, M., Grooß, J.-U., Woiwode, W., Johansson, S., Höpfner, M., Friedl-Vallon, F., Oelhaf, H., Preusse, P., Ungermann, J., Sinnhuber, B.-M., Ziereis, H., and Braesicke, P.: Nitrification of the lowermost stratosphere during the exceptionally cold Arctic winter 2015/16, Atmospheric Chemistry and Physics Discussions, https://doi.org/10.5194/acp-2019-108, 2019.

Carslaw, K. S., Luo, B. P., and Peter, T.: An analytical expression for the composition of aqueous {HNO$_3$-H$_2$SO$_4$-H$_2$O} stratospheric aerosols including gas phase removal of HNO$_3$, Geophys. Res. Lett., 22, 1877–1880, https://doi.org/10.1029/95GL01668, 1995.

Carslaw, K. S., Wirth, M., Tsias, A., Luo, B. P., Dörnbrack, A., Leutbecher, M., Volkert, H., Renger, W., Bacmeister, J. T., Reimer, E., and Peter, T.: Increased stratospheric ozone depletion due to mountain-induced atmospheric waves, Nature, 391, 675–678, https://doi.org/10.1038/35589, 1998.

Clerbaux, C., Boynard, A., Clarisse, L., George, M., Hadji-Lazaro, J., Herbin, H., Hurtmans, D., Pommier, M., Razavi, A., Turquety, S., Wespes, C., and Coheur, P.-F.: Monitoring of atmospheric composition using the thermal infrared IASI/MetOp sounder, Atmospheric Chemistry and Physics, 9, 6041–6054, https://doi.org/10.5194/acp-9-6041-2009, 2009.

de Laat, A. T. J. and van Weele, M.: The 2010 Antarctic ozone hole: Observed reduction in ozone destruction by minor sudden stratospheric warmings, Scientific Reports, 1, 38, https://doi.org/10.1038/srep00038, 2011.

de Zafra, R. and Smyshlyaev, S. P.: On the formation of HNO3 in the Antarctic mid to upper stratosphere in winter, Journal of Geophysical Research, 106, 23 115, https://doi.org/10.1029/2000JD000314, 2001.

Grooß, J. U., Engel, I., Borrmann, S., Frey, W., Günther, G., Hoyle, C. R., Kivi, R., Luo, B. P., Molleker, S., Peter, T., Pitts, M. C., Schlager, H., Stiller, G., Vömel, H., Walker, K. a., and Müller, R.: Nitric acid trihydrate nucleation and denitrification in the Arctic stratosphere, Atmospheric Chemistry and Physics, 14, 1055–1073, https://doi.org/10.5194/acp-14-1055-2014, 2014.

Hanson, D. and Mauersberger, K.: Laboratory studies of the nitric acid trihydrate: Implications for the south polar stratosphere, Geophysical Research Letters, 15, 855–858, https://doi.org/10.1029/GL015i008p00855, 1988.

Harris, N. R. P., Lehmann, R., Rex, M., and von der Gathen, P.: A closer look at Arctic ozone loss and polar stratospheric clouds, Atmospheric Chemistry and Physics, 10, 8499–8510, https://doi.org/10.5194/acp-10-8499-2010, 2010.

Hilton, F., Armante, R., August, T., Barnet, C., Bouchard, A., Camy-Peyret, C., Capelle, V., Clarisse, L., Clerbaux, C., Coheur, P.-F., Collard, A., Crevoisier, C., Dufour, G., Edwards, D., Faijan, F., Fourrié, N., Gambacorta, A., Goldberg, M., Guidard, V., Hurtmans, D., Illingworth, S., Jacquinet-Husson, N., Kerzenmacher, T., Klaes, D., Lavanant, L., Masiello, G., Matricardi, M., McNally, A., Newman, S., Pavelin, E., Payan, S., Péquignot, E., Peyridieu, S., Phulpin, T., Remedios, J., Schlüssel, P., Serio, C., Strow, L., Stubenrauch, C., Taylor, J., Tobin, D., Wolf, W., and Zhou, D.: Hyperspectral Earth Observation from IASI: Five Years of Accomplishments, Bulletin of the American Meteorological Society, 93, 347–370, https://doi.org/10.1175/BAMS-D-11-00027.1, 2012.

Hoffmann, L., Spang, R., Orr, A., Alexander, M. J., Holt, L. A., and Stein, O.: A decadal satellite record of gravity wave activity in the lower stratosphere to study polar stratospheric cloud formation, Atmospheric Chemistry and Physics, 17, 2901–2920, https://doi.org/10.5194/acp-17-2901-2017, 2017.

Höpfner, M., Luo, B. P., Massoli, P., Cairo, F., Spang, R., Snels, M., Di Donfrancesco, G., Stiller, G., von Clarmann, T., Fischer, H., and Biermann, U.: Spectroscopic evidence for NAT, STS, and ice in MIPAS infrared limb emission measurements of polar stratospheric clouds, Atmospheric Chemistry and Physics, 6, 1201–1219, https://doi.org/10.5194/acp-6-1201-2006, 2006.

Höpfner, M., Pitts, M. C., and Poole, L. R.: Comparison between CALIPSO and MIPAS observations of polar stratospheric clouds, Journal of Geophysical Research Atmospheres, 114, 1–15, https://doi.org/10.1029/2009JDO12114, 2009.

Hoyle, C. R., Engel, I., Luo, B. P., Pitts, M. C., Poole, L. R., Grooß, J. U., and Peter, T.: Heterogeneous formation of polar stratospheric clouds- Part 1: Nucleation of nitric acid trihydrate (NAT), Atmospheric Chemistry and Physics, 13, 9577–9595, https://doi.org/10.5194/acp-13- 9577-2013, 2013.

20

Hurtmans, D., Coheur, P.-F., Wespes, C., Clarisse, L., Scharf, O., Clerbaux, C., Hadji-Lazaro, J., George, M., and Turquety, S.: FORLI radiative transfer and retrieval code for IASI, Journal of Quantitative Spectroscopy and Radiative Transfer, 113, 1391–1408, https://doi.org/10.1016/j.jqsrt.2012.02.036, 2012.

James, A. D., Brooke, J. S. A., Mangan, T. P., Whale, T. F., Plane, J. M. C., and Murray, B. J.: Nucleation of nitric acid hydrates in polar stratospheric clouds by meteoric material, Atmospheric Chemistry and Physics, 18, 4519–4531, https://doi.org/10.5194/acp-18-4519- 2018, 2018.

Keys, J. G., Johnston, P. V., Blatherwick, R. D., and Murcray, F. J.: Evidence for heterogeneous reactions in the Antarctic autumn stratosphere, Nature, 361, 49–51, https://doi.org/10.1038/361049a0, 1993.

Klekociuk, A., Tully, M., Alexander, S., Dargaville, R., Deschamps, L., Fraser, P., Gies, H., Henderson, S., Javorniczky, J., Krummel, P., Petelina, S., Shanklin, J., Siddaway, J., and Stone, K.: The Antarctic ozone hole during 2010, Australian Meteorological and Oceanographic Journal, 61, 253–267, https://doi.org/10.22499/2.6104.006, 2011.

Koop, T., Luo, B., Tsias, A., and Peter, T.: Water activity as the determinant for homogeneous ice nucleation in aqueous solutions, Nature, 406, 611–614, https://doi.org/10.1038/35020537, 2000.

Kvissel, O. K., Orsolini, Y. J., Stordal, F., Isaksen, I. S. A., and Santee, M. L.: Formation of stratospheric nitric acid by a hydrated ion cluster reaction: Implications for the effect of energetic particle precipitation on the middle atmosphere, Journal of Geophysical Research: Atmospheres, 117, n/a–n/a, https://doi.org/10.1029/2011jd017257, 2012.

Lambert, A. and Santee, M. L.: Accuracy and precision of polar lower stratospheric temperatures from reanalyses evaluated from A-Train CALIOP andMLS, COSMIC GPS RO, and the equilibrium thermodynamics of supercooled ternary solutions and ice clouds, Atmospheric Chemistry and Physics, 18, 1945–1975, https://doi.org/10.5194/acp-18-1945-2018, 2018.

Lambert, A., Santee, M. L., Wu, D. L., and Chae, J. H.: A-train CALIOP and MLS observations of early winter Antarctic polar stratospheric clouds and nitric acid in 2008, Atmospheric Chemistry and Physics, 12, 2899–2931, https://doi.org/10.5194/acp-12-2899-2012, 2012.

Lambert, A., Santee, M. L., and Livesey, N. J.: Interannual variations of early winter Antarctic polar stratospheric cloud formation and nitric acid observed by CALIOP and MLS, Atmospheric Chemistry and Physics, 16, 15 219–15 246, https://doi.org/10.5194/acp-16-15219-2016, 2016.

Lawrence, Z. D., Manney, G. L., and Wargan, K.: Reanalysis intercomparisons of stratospheric polar processing diagnostics, Atmospheric Chemistry and Physics, 18, 13 547–13 579, https://doi.org/10.5194/acp-18-13547-2018, 2018.

Lowe, D. and MacKenzie, A. R.: Polar stratospheric cloud microphysics and chemistry, Journal of Atmospheric and Solar-Terrestrial Physics, 70, 13–40, https://doi.org/10.1016/j.jastp.2007.09.011, 2008.

Molleker, S., Borrmann, S., Schlager, H., Luo, B., Frey, W., Klingebiel, M., Weigel, R., Ebert, M., Mitev, V., Matthey, R., Woiwode, W., Oelhaf, H., Dörnbrack, A., Stratmann, G., Grooß, J.-U., Günther, G., Vogel, B., Müller, R., Krämer, M., Meyer, J., and Cairo, F.: Microphysical properties of synoptic-scale polar stratospheric clouds: in situ measurements of unexpectedly large HNO3-containing particles in the Arctic vortex, Atmospheric Chemistry and Physics, 14, 10 785–10 801, https://doi.org/10.5194/acp-14-10785-2014, 2014.

Murphy, D. M. and Koop, T.: Review of the vapour pressures of ice and supercooled water for atmospheric applications, Quarterly Journal of the Royal Meteorological Society, 131, 1539–1565, https://doi.org/10.1256/qj.04.94, 2005.

Peter, T.: Microphysics and heterogeneous chemistry of polar stratospheric clouds, Annual Review of Physical Chemistry, 48, 785–822, https://doi.org/10.1146/annurev.physchem.48.1.785, 1997.

Peter, T. and Grooß, J.-U.: Chapter 4. Polar Stratospheric Clouds and Sulfate Aerosol Particles: Microphysics, Denitrification and Heterogeneous Chemistry, in: Stratospheric Ozone Depletion and Climate Change, pp. 108–144, Royal Society of Chemistry, https://doi.org/10.1039/9781849733182-00108, 2012.

Piccolo, C. and Dudhia, A.: Precision validation of MIPAS-Envisat products, Atmospheric Chemistry and Physics, 7, 1915–1923, https://doi.org/10.5194/acp-7-1915-2007, 2007.

Pitts, M. C., Poole, L. R., Dörnbrack, A., and Thomason, L. W.: The 2009-2010 Arctic polar stratospheric cloud season: A CALIPSO perspective, Atmospheric Chemistry and Physics, 11, 2161–2177, https://doi.org/10.5194/acp-11-2161-2011, 2011.

Pitts, M. C., Poole, L. R., Lambert, A., and Thomason, L.W.: An assessment of CALIOP polar stratospheric cloud composition classification, Atmospheric Chemistry and Physics, 13, 2975–2988, https://doi.org/10.5194/acp-13-2975-2013, 2013.

Pitts, M. C., Poole, L. R., and Gonzalez, R.: Polar stratospheric cloud climatology based on CALIPSO spaceborne lidar measurements from 2006 to 2017, Atmospheric Chemistry and Physics, 18, 10 881–10 913, https://doi.org/10.5194/acp-18-10881-2018, 2018.

Rodgers, C. D.: Inverse Methods for Atmospheric Sounding - Theory and Practice, vol. 2 of Series on Atmospheric Oceanic and Planetary Physics, World Scientific Publishing Co. Pte. Ltd., https://doi.org/10.1142/9789812813718, 2000.

Ronsmans, G., Langerock, B., Wespes, C., Hannigan, J. W., Hase, F., Kerzenmacher, T., Mahieu, E., Schneider, M., Smale, D., Hurtmans, D., De Mazière, M., Clerbaux, C., and Coheur, P.-F.: First characterization and validation of FORLI-HNO3 vertical profiles retrieved from IASI/Metop, Atmospheric Measurement Techniques, 9, 4783–4801, https://doi.org/10.5194/amt-9-4783-2016, 2016.

Ronsmans, G.,Wespes, C., Hurtmans, D., Clerbaux, C., and Coheur, P.-F.: Spatio-temporal variations of nitric acid total columns from 9 years of IASI measurements – a driver study, Atmospheric Chemistry and Physics, 18, 4403–4423, https://doi.org/10.5194/acp-18-4403-2018, 2018.

Santee, M. L., Manney, G. L., Froidevaux, L., Read, W. G., and Waters, J. W.: Six years of UARS Microwave Limb Sounder HNO$_3$ observations : Seasonal, interhemispheric, and interannual variations in the lower stratosphere, Journal of Geophysical Research, 104, 8225–8246, https://doi.org/10.1029/1998JD100089, 1999.

Santee, M. L., Lambert, A., Read, W. G., Livesey, N. J., Cofield, R. E., Cuddy, D. T., Daffer, W. H., Drouin, B. J., Froidevaux, L., Fuller, R. A., Jarnot, R. F., Knosp, B. W., Manney, G. L., Perun, V. S., Snyder, W. V., Stek, P. C., Thurstans, R. P., Wagner, P. A., Waters, J. W., Muscari, G., de Zafra, R. L., Dibb, J. E., Fahey, D. W., Popp, P. J., Marcy, T. P., Jucks, K. W., Toon, G. C., Stachnik, R. A., Bernath, P. F., Boone, C. D., Walker, K. A., Urban, J., and Murtagh, D.: Validation of the Aura Microwave Limb Sounder HNO3 measurements, Journal of Geophysical Research, 112, 1–22, https://doi.org/10.1029/2007JD008721, 2007.

Schreiner, J., Voigt, C., Weisser, C., Kohlmann, A., Mauersberger, K., Deshler, T., Kröger, C., Rosen, J., Kjome, N., Larsen, N., Adriani, A., Cairo, F., Donfrancesco, G. D., Ovarlez, J., Ovarlez, H., and Dörnbrack, A.: Chemical , microphysical , and optical properties of polar stratospheric clouds, Journal of Geophysical Research, 108, 1–10, https://doi.org/10.1029/2001JD000825, 2003.

Schreiner, W., Rocken, C., Sokolovskiy, S., Syndergaard, S., and Hunt, D.: Estimates of the precision of GPS radio occultations from the COSMIC/FORMOSAT 3 mission, Geophysical Research Letters, 34, 1–5, https://doi.org/10.1029/2006GL027557, 2007.

Sheese, P. E., Walker, K. A., Boone, C. D., Bernath, P. F., Froidevaux, L., Funke, B., Raspollini, P., and von Clarmann, T.: ACE-FTS ozone, water vapour, nitrous oxide, nitric acid, and carbon monoxide profile comparisons with MIPAS and MLS, Journal of Quantitative Spectroscopy and Radiative Transfer, 186, 63–80, https://doi.org/10.1016/j.jqsrt.2016.06.026, 2017.

Snels, M., Scoccione, A., Liberto, L. D., Colao, F., Pitts, M., Poole, L., Deshler, T., Cairo, F., Cagnazzo, C., and Fierli, F.: Comparison of Antarctic polar stratospheric cloud observations by ground-based and space-borne lidar and relevance for chemistry–climate models, Atmospheric Chemistry and Physics, 19, 955–972, https://doi.org/10.5194/acp-19-955-2019, 2019.

Solomon, S.: Stratospheric ozone depletion: A review of concepts and history, Reviews of Geophysics, 37, 275–316, https://doi.org/10.1029/1999RG900008, 1999.

Spang, R., Hoffmann, L., Höpfner, M., Griessbach, S., Müller, R., Pitts, M. C., Orr, A. M. W., and Riese, M.: A multi-wavelength classification method for polar stratospheric cloud types using infrared limb spectra, Atmospheric Measurement Techniques, 9, 3619–3639, https://doi.org/10.5194/amt-9-3619-2016, 2016.

Spang, R., Hoffmann, L., Müller, R., Grooß, J.-U., Tritscher, I., Höpfner, M., Pitts, M., Orr, A., and Riese, M.: A climatology of polar stratospheric cloud composition between 2002 and 2012 based on MIPAS/Envisat observations, Atmospheric Chemistry and Physics, 18, 5089–5113, https://doi.org/10.5194/acp-18-5089-2018, 2018.

Toon, O. B., Hamill, P., Turco, R. P., and Pinto, J.: Condensation of HNO3 and HCl in the winter polar stratospheres, Geophysical Research Letters, 13, 1284–1287, https://doi.org/10.1029/GL013i012p01284, 1986.

Tritscher, I., Pitts, M. C., Poole, L. R., Alexander, S. P., Cairo, F., Chipperfield, M. P., et al.: Polar stratospheric clouds: Satellite observations, processes, and role in ozone depletion, Reviews of Geophysics, 59, e2020RG000702, https://doi.org/10.1029/2020RG000702.

Urban, J., Pommier, M., Murtagh, D. P., Santee, M. L., and Orsolini, Y. J.: Nitric acid in the stratosphere based on Odin observations from 2001 to 2009 – Part 1: A global climatology, Atmospheric Chemistry and Physics, 9, 7031–7044, https://doi.org/10.5194/acp-9-7031- 2009, 2009.

Voigt, C., Schreiner, J., Kohlmann, A., Zink, P., Mauersberger, K., Larsen, N., Deshler, T., Kro, C., Rosen, J., Adriani, A., Cairo, F., Donfrancesco, G. D., Viterbini, M., Ovarlez, J., Ovarlez, H., and David, C.: Nitric Acid Trihydrate (NAT) in Polar Stratospheric Clouds, Science, 290, 1756–1758, https://doi.org/10.1126/science.290.5497.1756, 2000.

Voigt, C., Larsen, N., Deshler, T., et al.: In situ mountainwave polar stratospheric cloud measurements: Implications for nitric acid trihydrate formation, J. Geophys. Res., 108(D5), doi:10.1029/2001JD001185, 2003.

Voigt, C., Schlager, H., Luo, B. P., Dörnbrack, A., Roiger, A., Stock, P., Curtius, J., Vössing, H., Borrmann, S., Davies, S., Konopka, P., Schiller, C., Shur, G., and Peter, T.: Nitric Acid Trihydrate (NAT) formation at low NAT supersaturation in Polar Stratospheric Clouds (PSCs), Atmospheric Chemistry and Physics, 5, 1371–1380, https://doi.org/10.5194/acp-5-1371- 2005, 2005.

von König, M.: Using gas-phase nitric acid as an indicator of PSC composition, Journal of Geophysical Research, 107, https://doi.org/10.1029/2001jd001041, 2002.

Wang, D. Y., Blom, C. E., Ward, W. E., Fischer, H., Blumenstock, T., Hase, F., Keim, C., Liu, G. Y., Mikuteit, S., Oelhaf, H., Wetzel, G., Cortesi, U., Mencaraglia, F., Bianchini, G., Redaelli, G., Pirre, M., Catoire, V., Huret, N., Vigouroux, C., Mahieu, E., Demoulin, P., Wood, S., Smale, D., Jones, N., Nakajima, H., Sugita, T., Urban, J., Murtagh, D., Boone, C. D., Bernath, P. F., Walker, K. a., Kuttippurath, J., Toon, G., Piccolo, C., Brunswick, N., Zealand, N., Science, S., and Cedex, P.: Validation of MIPAS HNO3 operational data, Atmospheric Chemistry and Physics, 7, 4905-4934, https://doi.org/10.5194/acp-7-4905-2007, 2007.

Wang, X. and Michelangeli, D. V.: A review of polar stratospheric cloud formation, China Particuology, 4, 261–271, https://doi.org/10.1016/S1672-2515(07)60275-9, 2006.

Wegner, T., Grooß, J.-U., von Hobe, M., Stroh, F., Sumin´ska-Ebersoldt, O., Volk, C. M., Hösen, E., Mitev, V., Shur, G., and Müller, R.: Heterogeneous chlorine activation on stratospheric aerosols and clouds in the Arctic polar vortex, Atmospheric Chemistry and Physics, 12, 11 095–11 106, https://doi.org/10.5194/acp-12-11095-2012, 2012.

Wespes, C., Hurtmans, D., Clerbaux, C., and Coheur, P.-F.: O_3 variability in the troposphere as observed by IASI over 2008-2016: Contribution of atmospheric chemistry and dynamics, Journal of Geophysical Research: Atmospheres, 122, 2429–2451, https://doi.org/10.1002/2016JD025875, http://doi.wiley.com/10.1002/2016JD025875, 2017.

WMO: Scientific Assessment of Ozone Depletion: 2014, Global Ozone Research and Monitoring Project – Report No. 55, World Meteorological Organization, Geneva, Switzerland, 2014.

Zhu, Y., Toon, O. B., Lambert, A., Kinnison, D. E., Brakebusch, M., Bardeen, C. G., Mills, M. J., and English, J. M.: Development of a Polar Stratospheric Cloud Model within the Community Earth System Model using constraints on Type I

PSCs from the 2010-2011 Arctic winter, Journal of Advances in Modeling Earth Systems, 7, 551–585, https://doi.org/10.1002/2015ms000427, 2015.

Zondlo, M. A., P. K. Hudson, A. J. Prenni, and M. A. Tolbert: Chemistry and microphysics of polar stratospheric clouds and cirrus clouds, Annu. Rev. Phys. Chem., 51, 473–499, 2000.